

Observed increase in the peak rain rates of monsoon depressions

S. Vishnu^{†1,*}, Mark D. Risser², Travis A. O'Brien^{3,2}, Paul A. Ullrich^{4,5}, and William R. Boos^{1,2}

¹Department of Earth and Planetary Science, University of California, Berkeley, CA, USA

²Climate and Ecosystem Sciences Division, Lawrence Berkeley National Laboratory, Berkeley, CA, USA

³Department of Earth and Atmospheric Sciences, Indiana University, Bloomington, IN, USA

⁴Department of Land, Air and Water Resources, University of California, Davis, Davis, CA, USA

⁵Computational Research Division, Lawrence Berkeley National Laboratory, Berkeley, CA, USA

*vishnuedv@gmail.com

ABSTRACT

Most extreme precipitation in the densely populated region of central India is produced by atmospheric vortices called monsoon lows and monsoon depressions. Here we use satellite and gauge-based precipitation estimates with atmospheric reanalyses to assess 40-year trends in the rain rates of these storms, which have remained unknown. We show that rain rates increased in the rainiest quadrant of monsoon depressions, southwest of the vortex center; precipitation decreased in eastern quadrants, yielding no clear trend in precipitation averaged over the entire storm diameter. In an atmospheric reanalysis, ascent increased in the region of amplifying precipitation, but we could not detect trends in the intensity of rotational winds around the storm center. These storm changes occurred in a background environment where humidity increased rapidly over land while warming was more muted. Monsoon lows, which we show produce less precipitation than depressions, exhibit weaker trends that are less statistically robust.

Introduction

More than one billion people rely on water delivered by the South Asian monsoon, which produces about 80% of the Indian subcontinent's annual precipitation¹. Monsoon precipitation in this densely populated region can be highly concentrated in time, with more than 15 cm of rain falling on a single day at least once every few years over large parts of central India, the Himalayas, and India's west coast (Fig. 1a, b). Over central India, nearly all of this extreme precipitation is produced by monsoon low-pressure systems (LPS; Fig. 1b), which are transient atmospheric vortices with outer diameters near 2000 km. Around 15 of these vortices form on average each summer, with genesis occurring most often over the northern Bay of Bengal; the systems then propagate to the northwest over India, Nepal, and Pakistan (Fig. 1c), where they produce abundant rain despite their modest surface wind speeds^{2–4}.

Extreme precipitation events in central India increased in frequency over the last half-century^{5,6}, and the growth of population density in this region compounded the associated increase in human exposure to hydrological extremes (Fig. 1a, b, d). Previous studies argued that this increase in extreme rainfall may be due to the activity of LPS changing in a somewhat complex fashion. Specifically, the number of weak LPS (monsoon lows) was found to have increased while the number of stronger LPS (monsoon depressions) declined^{7–10}. However, more recent studies found that this apparent decline in the number of monsoon depressions may be an artifact of changes in the observing network used to produce the hand-analyzed dataset of LPS counts on which those claims were based^{11,12}. In five atmospheric reanalyses, the number and cumulative lifetime of lows and depressions do not show any detectable trend in the last 40 years¹², and no trend could be detected in a satellite scatterometer estimate of synoptic-event frequency over a similar period¹¹.

Since LPS are detected and classified as lows or depressions based on wind speeds and surface pressure anomalies, rather than rain rates (see Methods), this raises the question of how rain rates in lows and depressions differ and how these rain rates have changed over time. Prior work has not examined these straightforward questions. Some studies have associated changes in extreme rainfall with changes in LPS counts and LPS track locations^{6,13}, but these studies did not assess whether the precipitation rates of LPS have changed in the observational record. Thus, we lack an assessment of precipitation trends in

[†]Current affiliation: Météo-France, Direction de la Climatologie et des Services Climatiques, Toulouse, France & Institute of Research for Development (IRD): Nouméa, New-Caledonie

36 the dominant storm type in Earth's most densely populated region. With this motivation, our main goal here is to determine
37 whether the precipitation in LPS has changed in recent decades, as global mean temperature has risen. As a related task, we
38 also assess how the rain rate of monsoon lows differs from that of monsoon depressions. We discuss possible causes of these
39 changes, recognizing that trends in extreme precipitation are often influenced by trends in vertical structures of temperature and
40 humidity that are difficult to observe.

41 Results

42 Importance of monsoon depressions for extreme rain

43 We begin by creating storm-centered composites of rain rates in monsoon lows and depressions, using a storm-track dataset
44 that was compiled with a well-validated algorithm for LPS detection and classification¹². This novel analysis allows us to
45 confirm that the multiple datasets we use here reproduce the well-known spatial structure of precipitation in LPS^{14–16} while
46 also providing a baseline spatial structure against which to assess trends.

47 In vortex-centered composites based on tracks obtained from our optimized tracking algorithm applied to an atmospheric
48 reanalysis¹², we confirm that 2 satellite datasets, 2 rain-gauge datasets, and reanalyzed precipitation all reproduce the well-
49 known spatial structure of peak precipitation occurring about 200 km southwest of the vortex center (Fig. 2a-e). Depressions
50 produce more rain than lows, at peak rates up to 80% higher in composite means (stippling in Fig. 2a-e).

51 When averaged spatially over an 8-degree radius around the vortex center (an optimal radius for associating rainfall with
52 LPS¹⁷), instantaneous rain rates in depressions are only about 20% higher than those in lows (Fig. 2f). However, when
53 precipitation is accumulated along the tracks of storms, depressions produce nearly double the rainfall of lows (Fig. 2g).
54 This occurs because depressions are longer-lived, and total accumulated LPS rainfall is highly correlated with LPS lifetime
55 (Pearson's $r = 0.89$; Supplementary Fig. S1). These properties of the precipitation histograms hold across all five precipitation
56 datasets examined here (Supplementary Fig. S2), and show that most extreme precipitation in central India (~ 320 events/year,
57 with ~ 237 events/year occurring within 8° radius of an LPS) is produced by monsoon depressions (~ 187 count/year) rather
58 than lows (~ 50 count/year).

59 Increase in monsoon depression rain rates

60 We now assess whether LPS precipitation rates have changed in the observational record. Vortex-centered maps of linear trends
61 show that precipitation rates in monsoon depressions have increased by $2\text{--}6 \text{ mm day}^{-1} \text{ decade}^{-1}$ in the southwest quadrant of
62 these storms, close to the location of the precipitation peak which has a magnitude around 30 mm day^{-1} in most datasets (Fig.
63 3a-e; relative rates of change are examined below). This increase passes a false discovery rate (FDR) test (see Methods) in 4 of
64 our 5 precipitation datasets. The trend did not pass the FDR test in the PERSIANN dataset, which is generated from infrared
65 satellite data using neural networks and incorporates rain gauge data indirectly only through adjustment to the monthly-mean,
66 2.5° -resolution GPCP dataset (PERSIANN is thus our only dataset that does not directly incorporate rain gauge observations).
67 Monsoon lows exhibit a weaker increase that is less spatially focused and only passes an FDR test in 2 of the 5 datasets
68 (Supplementary Fig. S3a-e); this, along with the greater importance of depressions for extreme rainfall (discussed above), is
69 why we focus primarily on trends in monsoon depression precipitation. When averaged over the western half of the storm
70 center, the rain rate increases in depressions amount to a relative change of $2\text{--}7\% \text{ decade}^{-1}$, although the 90% confidence
71 intervals on these changes span a wider range and the increase is only statistically distinct from zero in 3 of the 5 precipitation
72 datasets (Fig. 4a).

73 We also assess trends of point-wise precipitation in LPS using a statistical model of extreme rainfall. Specifically, for each
74 year of each dataset, we fit a single gamma distribution to the spatially resolved precipitation rates in the western half of LPS
75 (because the peak precipitation occurs in the western half of the composite-mean storm), then examine how these gamma fits
76 change over time (see Methods; gamma distributions are often used to represent precipitation intensities, for statistical and
77 physical reasons^{18,19}). Over the past 40 years in each observational record, these gamma fits show a reduction in the occurrence
78 of lower rain rates and an increase in the occurrence of higher rain rates. In these statistical distributions, the transition between
79 decreasing and increasing frequency lies between $30\text{--}60 \text{ mm day}^{-1}$ depending on the dataset (Fig. 3f), well below the 150 mm
80 day^{-1} threshold that is often used to classify precipitation as extreme. Qualitatively similar changes in gamma fits occur for
81 monsoon lows, although one dataset (PERSIANN) exhibits a decrease in the probability of rain rates larger than about 60 mm
82 day^{-1} in the lows (Supplementary Fig. S3f).

83 There is a decrease in rain rates on the eastern side of the systems in the ERA5 and IMD datasets, although in the latter this
84 is strongest to the northeast of the storm center while in ERA5 the decrease is focused in the southeast quadrant. Any decrease
85 in the CHIRPS and PERSIANN datasets does not pass our statistical tests for significance. For monsoon lows, no reduction in
86 rain rates is detected in any of the datasets (Supplementary Fig. S3). When rain rates are averaged horizontally over an 8° radius
87 around the center of monsoon depressions, these reductions on the eastern side of the storms offset the increase on the western
88 side to produce trends that are indistinct from zero in most of the datasets (Fig. 4a). The lower-resolution version of the IMD

dataset has a decrease of about 5% decade⁻¹ in this storm-averaged metric, but given its difference with the higher-resolution IMD dataset (which includes larger number of station observations), we view that result with caution. Precipitation trends averaged horizontally over monsoon lows are indistinct from zero in all five datasets (Supplementary Fig. S4a).

The observed increase in extreme precipitation events over central India (Fig. 1d) can be attributed to the increase in rain rates of LPS as follows. The number of extreme precipitation events in the last twenty years of our analysis period (2000–2019) is larger by 84 events/year compared to the mean of the first twenty years (1979–1998). We associate a rain event with an LPS when it occurs within an 8° radius of an LPS center; this allowed us to determine that LPS account for an increase of 61 events/year between these two epochs. Of that number, approximately 40 events/year come from monsoon depressions, while lows contribute the remaining 21 events/year. Thus, LPS precipitation can account for the majority of the observed intensification of extreme rainfall events over central India in recent decades.

Changes in storm environment and dynamics

We now assess changes in the large-scale environment of monsoon LPS and in the structure and intensity of these storms, with the goal of determining whether the rain rate changes discussed above can be attributed to any changes in storm or environmental properties.

The Indian Ocean has warmed over the past century^{20,21}, but during boreal summer this warming has been largest on the equator with comparatively little change in the northernmost Indian Ocean and much of India^{22,23}. Indeed, no trend in surface air temperature can be detected over the last 40 years in central India and the northern Bay of Bengal, where the vast majority of LPS tracks and genesis points lie (Fig. 5a). If the relative changes in monsoon depression precipitation are normalized by the seasonal-mean temperature change averaged over the tropical Indian Ocean, trends in the雨iest part of the storms increase at large rates of about 10–40% K⁻¹, but with uncertainty intervals that are large enough to include typical Clausius-Clapeyron rates (e.g. 7% K⁻¹) in nearly all of the datasets (Fig. 4b). Computing these relative rates of change using temperatures averaged over different regions produces similar results (Supplementary Fig. S5).

In contrast to the muted warming seen over much South Asian land, humidity has increased rapidly over India and adjacent countries. When humidity and temperature changes are expressed in terms of their contribution to the change in atmospheric energy content, the humidity increase over large parts of South Asia exceeds the energy change associated with a 1 K decade⁻¹ warming, and is several times larger than either the local warming or the remote warming over the equatorial Indian Ocean (Fig. 5b). Although this humidity trend is obtained from the ERA5 atmospheric reanalysis, which assimilates input from an evolving observing network, a consistent increase in surface air specific humidity is found in station data (albeit at coarser spatial resolution; black contour in Fig. 5b). The highest humidity increase lies over northwest India, in a region where intrusions of dry air have been argued to suppress monsoon depression rainfall²⁴. By that mechanism, one would expect this observed humidity increase to enhance monsoon depression rainfall. This humidity increase is also apparent when trends are evaluated in a storm-centered reference frame, showing that surface air specific humidity has increased most rapidly in the northern quadrants of monsoon depressions (Fig. 6a). A similar pattern of change in the vortex-centered composite for monsoon lows (Supplementary Fig. S6a) further supports the hypothesis that this pattern results from the environment through which LPS propagate; the seasonal-mean humidification is largest to the north of the region of highest track density for LPS (Fig. 5b).

When averaged over the heavily precipitating region of monsoon depressions, the surface air specific humidity has increased at a rate of about 1% decade⁻¹, which is several times smaller than the 2–7% decade⁻¹ rate of increase of precipitation in that region (Fig. 4a). However, uncertainty estimates on these rates of precipitation increase are large, as mentioned above, and in 4 out of 5 of the precipitation datasets these uncertainty intervals overlap the central estimate of the humidity increase. Furthermore, it may be more appropriate to compare the precipitation change near the storm center with the humidity increase on the poleward side of the vortex center, since idealized convection-permitting simulations of monsoon depressions show that precipitating air parcels in these storms originate several hundred km north of the heavily precipitating region²⁵. But choosing the most appropriate vertical level and horizontal location for such a comparison is difficult, at best; given this difficulty and the large uncertainty of the precipitation rate changes, we do not further refine the regions used for quantitative comparison of the humidity and precipitation trends.

Examination of wind changes in a storm-centered reference frame reveals a large increase in ascent in the heavily precipitating region of depressions (Fig. 6b). This composite mean rate of increase of ascent is several times greater than that of specific humidity (approximately 4% decade⁻¹ compared to 1% decade⁻¹), although the uncertainty is again large enough that the difference is not statistically significant (Fig. 4a). The enhanced ascent extends through the full troposphere in the heavily precipitating region (Supplementary Fig. S7c), and has horizontal structure that is insensitive to the choice of layer in the lower troposphere. Understanding of changes in vertical motion can sometimes be gained from assessing changes in the vertical thermodynamic structure^{26–28}. However, such trends in reanalyses may be heavily biased by changes in the observing network²⁹ (the same is true of the trend in vertical motion shown in Fig. 6b), and it is difficult, at best, to obtain direct observations of upper-level temperatures and humidities at sufficient spatiotemporal resolution to create storm-centered

composites of such trends. With this caveat, we examined vertical structures of trends and found a mid-tropospheric warming in the composite monsoon depression, implying an increase in static stability, and a complex vertical structure in the specific humidity trend consisting of a mid-tropospheric moistening above a weak lower-tropospheric drying and the aforementioned surface air moistening (Supplementary Fig. S7a, b). In the absence of any change in vertical motion, the increase in static stability would require an increase in diabatic heating (i.e. in precipitation) to maintain balance in the thermodynamic equation, given the weak horizontal temperature gradients at these latitudes³⁰; because the reanalysis exhibits an increase in ascent extending through the full troposphere (Supplementary Fig. S7c), an even larger increase in precipitation is required to maintain thermodynamic balance. Altogether, this means the thermodynamic balance is underconstrained, with three variables changing concurrently, so we must turn to other constraints to understand causation.

For quasigeostrophic dynamics, which have been shown to be relevant to monsoon depressions^{16,31}, a constraint on vertical motion and precipitation was obtained by deriving a nonlinear relation between precipitable water and rain rates, and showing this described global climate model projections of extreme precipitation in synoptic-scale storms in general³². Simulations of 10 observed LPS in a regional, convection-permitting model found that precipitation increased at twice the relative rate of specific humidity in response to an imposed uniform warming, with vertical velocity and the intensity of the surface low pressure both increasing³³. In observations, intrusions of dry air from the deserts of southwestern Asia have been shown to reduce upward motion on the western side of monsoon depressions²⁴, so the moistening of northwestern India would be expected to produce the enhanced precipitating ascent that we found on the western side of these storms.

Metrics for the intensity of the rotational flow in LPS show no discernible changes. We find no statistically significant linear trend in the spatial maximum of surface wind speed or in the difference in mean sea level pressure (MSLP) between the storm center and its surroundings (Fig. 4). Since both the peak surface wind speed and this MSLP difference are used to classify the intensity of LPS (see Methods section), they are the most obvious measures of storm intensity to assess. We also examine trends in the difference in streamfunction of the 850 hPa horizontal wind between the storm's center and its surroundings, which provides a measure of the strength of the rotational flow around the storm at 850 hPa; this metric also does not exhibit a detectable trend. When trends in 850 hPa horizontal winds are examined in a storm-centered reference frame, the only statistically significant change is an increase in westward flow on the northern side of the vortex (Fig. 6c). It is unclear whether rotational flow does increase on other sides of the storm but is simply not statistically detectable, or whether this constitutes a change in storm structure.

Might a shift in the tracks of monsoon depressions have caused some of these changes, e.g. by altering the position of the storms relative to topographic features? A recent study did argue that a southward shift in LPS tracks caused an increase in extreme precipitation over central India, together with a decrease north of that region¹³. We find that an amplification of peak rain rates in monsoon depressions is still detected when storms are sampled only within the southern or northern boxes used in that study (Supplementary Fig. S8). Thus, the increase in monsoon depression rain rates seems to have occurred together with any meridional shift in their tracks.

Discussion

Despite the importance of monsoon lows and depressions for South Asian hydrology^{34–36}, observed trends in the precipitation rates of these storms had not been quantified. This knowledge gap was problematic because prior studies made the claim that monsoon depression frequency had decreased strongly while extreme precipitation increased over central India^{7–10}; the number of heavily precipitating lows was assumed to be increasing, or the precipitation rate of lows was assumed to be rising, to allow this to occur. However, the rain rates of lows and depressions had not been separately quantified until now.

Our findings provide a simple explanation for the observed increase in extreme precipitation over central India: the peak precipitating ascent in monsoon depressions amplified over the past 40 years, in an environment where specific humidity has rapidly increased. Depressions rain more than lows, and precipitation trends in depressions are thus most relevant for trends in extreme rainfall. This argument is consistent with the recent finding that any decline in monsoon depression frequency has been comparatively small and perhaps an artifact of the introduction of satellite data into the observing network^{11,12}. Our analyses do not clearly establish a causal relation between the changes in humidity and precipitation, but it does not seem plausible that an increase in rain rates of LPS would cause the widespread seasonal-mean humidification seen over nearly all of South Asia (Fig. 5b).

The increased peak rain rates that we find in monsoon depressions may be distinct from those expected if LPS winds and relative humidities remained unchanged while the atmosphere warmed. Such a Clausius-Clapeyron scaling approximately describes next-century projected changes in simulated extratropical precipitation extremes^{27,37,38} and next-century changes in simulated tropical cyclone (TC) precipitation when TC intensity is controlled for^{39,40}. In contrast, while global climate model projections of tropical precipitation extremes remain highly uncertain, higher sensitivities to temperature have been projected for tropical extremes, with intensification of vertical winds accompanying warming-induced increases in specific humidity^{27,41,42}. A positive feedback between upward motion and the latent heating produced by precipitation has been

proposed to amplify some types of extreme precipitation at a faster rate, particularly when the precipitation is produced by moist convection^{38,43}. Some studies have argued that precipitating ascent in monsoon depressions should increase more rapidly than the environmental humidity because of a positive feedback between low-level moisture convergence and precipitation³³, but that feedback relies on transient depletion of a large reservoir of convective available potential energy (CAPE) and, when formulated mathematically, produces runaway growth at the shortest spatial scales^{28,44,45}. Instead, super-Clausius-Clapeyron scaling of extreme rainfall may result from a stable, self-limiting positive feedback between enhanced latent heating and ascent that occurs when the environmental specific humidity increases³². Such interaction would be consistent with the concurrent increase in humidity and ascent found here, in the absence of detectable changes in vortex strength.

Although one might expect the vertical motion and rotational flow in monsoon LPS to intensify concurrently, recent work has indicated that these two components of the circulation can evolve at least somewhat independently. Baroclinic and barotropic instabilities were both long ago hypothesized to cause the amplification of LPS, but recent work has shown that barotropic growth due to meridional shear of the low-level zonal wind likely dominates^{46,47}. This barotropic growth seems to require interaction with latent heating⁴⁸, which in turn is enhanced by cyclonic flow advecting moisture in a background moisture gradient^{25,49}. In a shallow water model, the precipitation and rotational winds in idealized monsoon LPS intensified at different rates as the background gradients of humidity and zonal wind were altered⁵⁰. In observational analyses, barotropic energy conversion (from the background meridional shear of the zonal wind) was found to amplify LPS rotational winds^{51,52}, while meridional advection of humidity was associated with the growth of moist static energy anomalies in LPS⁵³. Thus, it seems possible that a broad humidification of South Asian land might enhance precipitating ascent in monsoon LPS while producing little change in their rotational winds. This is consistent with the lack of any large change in the meridional gradient of seasonal-mean absolute vorticity (Supplementary Fig. S9); a change in sign of this gradient is a necessary criterion for barotropic instability.

It is unclear how these observed changes, assessed over the last 40 years, will relate to future LPS changes driven by greenhouse gas-induced warming. Historical warming may have been offset over Asia by aerosol-induced cooling⁵⁴, and perhaps also by land use changes such as increased irrigation^{55–58}. Nevertheless, the observed trends analyzed here quantify the association of monsoon LPS precipitation with regional humidity changes, and can serve as a reference for climate model simulations of the historical past and of future decades.

Methods

Data sources

LPS tracks

Monsoon low-pressure system (LPS) tracks for boreal summer (June-September) 1979-2019 were obtained from a Zenodo archive⁵⁹ produced under a previous study that devised an optimized, objective algorithm for identifying LPS in multiple atmospheric reanalyses¹². We used LPS tracks from ERA5, the latest reanalysis from the European Centre for Medium-Range Weather Forecasts^{29,60}. LPS are categorized into weaker monsoon lows and stronger monsoon depressions based on their intensities: lows have surface wind speeds less than 8.5 ms^{-1} and central mean sea level pressure (MSLP) at least 2 hPa lower than surrounding regions, while depressions have wind speeds $8.5\text{--}13.5 \text{ ms}^{-1}$ and MSLP at least lower than 4 hPa than the surrounding. More details on the detection and classification of LPS are provided by the study that devised the optimized tracking algorithm¹². The ERA5 track data for depressions agrees well with the IMD track dataset¹². We use the ERA5 dataset because it was produced using an objective algorithm that remained unchanged over its decades-long period, and because it includes monsoon lows (which are excluded by the IMD dataset).

Population density

We used global population density estimates from the fourth version of the Gridded Population of the World (GPWv.4), which estimates the distribution of human population at 15 arc-minute resolution⁶¹. The dataset is based on national censuses and is adjusted to match the 2015 Revision of the United Nation's World Population Prospects (UN WPP) country totals for the years 2000, 2005, 2011, 2015, and 2020⁶².

Precipitation and atmospheric variables

We analyzed five rainfall datasets in this work: (i) hourly, $0.25^\circ \times 0.25^\circ$ horizontal resolution precipitation from ERA5⁶⁰, which incorporates newly reprocessed observations and input from more recent instruments that were not assimilated older reanalyses^{29,60}, (ii) daily gridded precipitation over the Indian region at a horizontal resolution of 0.25° from the India Meteorological Department (IMD)⁶³ based on rain gauges, with over 3,000 stations contributing data for our analysis period of 1979-2019⁶³, (iii) daily gridded precipitation over the Indian region at a horizontal resolution of 1° from the IMD⁶⁴, based on a fixed 1,803 rain gauges (to minimize effects of temporal heterogeneity in the observing network) for the period of 1979-2019, (iv) daily precipitation from the Climate Hazards group Infrared Precipitation with Stations (CHIRPS)⁶⁵, which is based

on both rain gauges and satellite data, has a horizontal resolution of 0.25° , and is available for the years 1981-2019, (v) daily precipitation at a horizontal resolution of 0.25° from the Precipitation Estimation from Remotely Sensed Information using Artificial Neural Networks Climate Data Record (PERSIANN-CDR)⁶⁶ for 1982-2019; this dataset is based on satellite observations, but is adjusted toward the Global Precipitation Climatology Project (GPCP), which is in turn based on both rain gauges and satellite data.

To characterize the dynamic and thermodynamic state of LPS as well as the seasonal-mean background conditions, we used surface-air temperature, surface-air specific humidity, and lower tropospheric vertical wind (700-925 hPa) and horizontal wind (850 hPa) from ERA5⁶⁰. We also used monthly mean temperatures and humidities from over 4,500 quality-controlled stations, supplied as a global gridded product in the HADISDH dataset^{67,68}.

Analysis methods

Extreme rainfall over a grid point of the IMD dataset at a horizontal resolution of 0.25° is defined as values at that point equal to or exceeding 15 cm day^{-1} , consistent with several prior studies^{5,6}. Although we used a fixed threshold for extreme events, percentile-based and threshold-based measures provide qualitatively similar estimates of variability over the central Indian region⁶. Consistent with World Meteorological Organization guidelines⁶⁹, we used an absolute threshold rather than a percentile-based measure because the former better represents disaster-causing events.

All linear trends were computed using an iterative robust linear model that downweights outliers, as implemented in the Python statsmodels module⁷⁰. Two-tailed p -values were obtained from the t -statistics of the linear model parameters. To aid in correctly interpreting multiple simultaneous statistical tests in the maps of trends, we use these p -values in a false discovery rate (FDR) test^{71,72} with two rate thresholds: 0.15 and 0.33. Areas that are point-wise statistically significant by a standard t-test at a typical 0.05 or 0.10 confidence level are much more spatially extensive than areas passing the FDR test in the maps shown here.

Vortex-centered composites (e.g. of precipitation, humidity, and vertical motion) are produced by averaging in a latitude-longitude coordinate system centered on the vortex center. Averages are first taken over all time steps within a storm and then over all storms. Trends are computed from the storm averaged composites regressed against the time of each storm for the period of 1979-2019.

The procedure for computing a vortex-centered rainfall composite depends on the temporal resolution of the rainfall dataset. ERA5 provides precipitation at hourly resolution, so we use hourly LPS positions for that dataset. The other datasets all provide precipitation at daily resolution, so we use LPS locations at midday (1200 UTC) for composite analyses. However, the IMD dataset represents accumulated rainfall from 0300 UTC of the previous day to 0300 UTC of the current day, so the track point is chosen at 1500 UTC of the previous day for consistency.

Being based on rain gauge data, the IMD datasets provide precipitation for land areas only. Therefore, only track locations over land were used for LPS composites based on the IMD datasets. To evaluate the consistency between those land-only datasets and the datasets available over both land and ocean, we computed monsoon depression precipitation trends in ERA5 separately using data from land points only and from all land and ocean points; these rainfall trends are highly consistent with each other (Supplementary Fig. S10).

A statistical model was constructed for precipitation within LPS by fitting a gamma distribution to the storm-centered rain rates in the western half of the storm ($5^\circ\text{S}-5^\circ\text{N}$, $5^\circ\text{W}-0^\circ\text{E}$ in vortex-centered coordinates). The rain rates used in this fit were the spatially resolved (i.e. point-wise) rain rates averaged over all times within each LPS, with only rates greater than 0.2 mm day^{-1} used in the fit; one gamma distribution was fit to these rain rates for all storms in each year of each precipitation dataset. This yielded one value for each year for each parameter of the gamma distribution, and a linear fit as a function of time (i.e. year) was then made to these parameters. The change in probabilities shown in Fig. 3f and Supplementary Fig. S3f is the difference between the gamma distributions constructed from the temporal endpoints of these linear fits to the time series of parameter values.

LPS-averaged rainfall, as displayed in Fig. 2f, g and Supplementary Fig. S2, is the precipitation averaged horizontally over a circle of radius 8° around the vortex center. Previous work found the radius of 8° to be appropriate for attributing precipitation to LPS¹⁷. Monsoon low and monsoon depression rainfall are the time-average of all time steps over the entire life of the vortex.

DATA AVAILABILITY

The monsoon Low-pressure system track data is obtained from the Zenodo archive (<https://zenodo.org/record/389064#.ZAmSIi9U1QI>). The ERA5 data set was obtained from the Copernicus Climate Change Service Climate Data Store (CDS) website (at <https://cds.climate.copernicus.eu/cdsapp#!/>), accessed on 1 March 2021. The India Meteorological Department record of rainfall was downloaded from the IMD website at https://www.imdpune.gov.in/cmpg/Griddata/Rainfall_25_Bin.html and https://www.imdpune.gov.in/cmpg/Griddata/Rainfall_1_NetCDF.html. Daily precipitation from the Climate Hazards Group Infrared Precipitation with Stations (CHIRPS) accessed from <https://data.chc.ucsb.edu/products/CHIRPS-2.0/>. Precipita-

302 tion Estimation from Remotely Sensed Information using Artificial Neural Networks Climate Data Record (PERSIANN-CDR)
303 data downloaded from <https://www.ncei.noaa.gov/data/precipitation-persiann/access/>. The hu-
304 midity data from the HADISDH is available at <https://www.metoffice.gov.uk/hadobs/hadisdh/>. All data
305 used in the paper are appropriately acknowledged in the method section.

306 CODE AVAILABILITY

307 The Codes to produce the figures are available from the corresponding author with proper request.

308 References

- 309 1. Parthasarathy, B., Munot, A. A. & Kothawale, D. R. All-India monthly and seasonal rainfall series: 1871–1993. *Theor.
310 Appl. Climatol.* **49**, 217–224 (1994).
- 311 2. Sikka, D. Some aspects of the life history, structure and movement of monsoon depressions. In *Monsoon dynamics*,
312 1501–1529 (Springer, 1978).
- 313 3. Mooley, D. A. & Shukla, J. *Characteristics of the westward-moving summer monsoon low pressure systems over the Indian
314 region and their relationship with the monsoon rainfall* (University of Maryland, Department of Meteorology, Center for
315 Ocean-Land . . . , 1987).
- 316 4. Sikka, D. *A study on the monsoon low pressure systems over the Indian region and their relationship with drought and
317 excess monsoon seasonal rainfall* (Center for Ocean-Land-Atmosphere Studies, Center for the Application of . . . , 2006).
- 318 5. Goswami, B. N., Venugopal, V., Sengupta, D., Madhusoodanan, M. & Xavier, P. K. Increasing trend of extreme rain events
319 over India in a warming environment. *Science* **314**, 1442–1445 (2006).
- 320 6. Roxy, M. K. *et al.* A threefold rise in widespread extreme rain events over central India. *Nat. communications* **8**, 1–11
321 (2017).
- 322 7. Ajayamohan, R. S., Merryfield, W. J. & Kharin, V. V. Increasing trend of synoptic activity and its relationship with extreme
323 rain events over central India. *J. Clim.* **23**, 1004–1013 (2010).
- 324 8. Rajeevan, M., De, U. & Prasad, R. Decadal variation of sea surface temperatures, cloudiness and monsoon depressions in
325 the north Indian ocean. *Curr. Sci.* **79**, 283–285 (2000).
- 326 9. Patwardhan, S. & Bhalme, H. A study of cyclonic disturbances over India and the adjacent ocean. *Int. J. Climatol. A J.
327 Royal Meteorol. Soc.* **21**, 527–534 (2001).
- 328 10. Jadhav, S. & Munot, A. Warming SST of Bay of Bengal and decrease in formation of cyclonic disturbances over the Indian
329 region during southwest monsoon season. *Theor. applied climatology* **96**, 327–336 (2009).
- 330 11. Cohen, N. Y. & Boos, W. R. Has the number of Indian summer monsoon depressions decreased over the last 30 years?
331 *Geophys. Res. Lett.* **41**, 7846–7853 (2014).
- 332 12. Vishnu, S., Boos, W. R., Ullrich, P. A. & O'Brien, T. A. Assessing historical variability of South Asian monsoon lows and
333 depressions with an optimized tracking algorithm. *J. Geophys. Res. Atmospheres* **125**, e2020JD032977 (2020).
- 334 13. You, Y. & Ting, M. Observed trends in the south Asian monsoon low-pressure systems and rainfall extremes since the late
335 1970s. *Geophys. Res. Lett.* **48**, e2021GL092378 (2021).
- 336 14. Godbole, R. V. The composite structure of the monsoon depression. *Tellus* **29**, 25–40 (1977).
- 337 15. Saha, K. & Chang, C. The baroclinic processes of monsoon depressions. *Mon. weather review* **111**, 1506–1514 (1983).
- 338 16. Sanders, F. Quasi-geostrophic diagnosis of the monsoon depression of 5–8 July 1979. *J. Atmospheric Sci.* **41**, 538–552
339 (1984).
- 340 17. Hunt, K. M. & Fletcher, J. K. The relationship between Indian monsoon rainfall and low-pressure systems. *Clim. Dyn.* **53**,
341 1859–1871 (2019).
- 342 18. Thom, H. C. A note on the gamma distribution. *Mon. weather review* **86**, 117–122 (1958).
- 343 19. Martinez-Villalobos, C. & Neelin, J. D. Why do precipitation intensities tend to follow gamma distributions? *J. Atmospheric
344 Sci.* **76**, 3611–3631 (2019).
- 345 20. Levitus, S., Antonov, J. I., Boyer, T. P. & Stephens, C. Warming of the world ocean. *Science* **287**, 2225–2229 (2000).
- 346 21. Alory, G., Wijffels, S. & Meyers, G. Observed temperature trends in the Indian ocean over 1960–1999 and associated
347 mechanisms. *Geophys. Res. Lett.* **34** (2007).

- 348 22. Chung, C. E. & Ramanathan, V. Weakening of north indian sst gradients and the monsoon rainfall in india and the sahel. *J. Clim.* **19**, 2036–2045 (2006).
- 349 23. Roxy, M. K., Ritika, K., Terray, P. & Masson, S. The curious case of indian ocean warming. *J. Clim.* **27**, 8501–8509 (2014).
- 350 24. Fletcher, J. K., Parker, D. J., Hunt, K. M., Vishwanathan, G. & Govindankutty, M. The interaction of Indian monsoon depressions with northwesterly midlevel dry intrusions. *Mon. Weather. Rev.* **146**, 679–693 (2018).
- 351 25. Diaz, M. & Boos, W. R. Evolution of idealized vortices in monsoon-like shears: Application to monsoon depressions. *J. Atmospheric Sci.* **78**, 1207–1225 (2021).
- 352 26. Neelin, J. D. *et al.* Precipitation extremes and water vapor. *Curr. Clim. Chang. Reports* 1–17 (2022).
- 353 27. O’Gorman, P. A. Precipitation extremes under climate change. *Curr. climate change reports* **1**, 49–59 (2015).
- 354 28. Emanuel, K. A., David Neelin, J. & Bretherton, C. S. On large-scale circulations in convecting atmospheres. *Q. J. Royal Meteorol. Soc.* **120**, 1111–1143 (1994).
- 355 29. Hersbach, H. & Dee, D. ERA5 reanalysis is in production, ECMWF Newsletter 147, ECMWF. *Reading, UK* (2016).
- 356 30. Sobel, A. H., Nilsson, J. & Polvani, L. M. The weak temperature gradient approximation and balanced tropical moisture waves. *J. atmospheric sciences* **58**, 3650–3665 (2001).
- 357 31. Boos, W., Hurley, J. & Murthy, V. Adiabatic westward drift of Indian monsoon depressions. *Q. J. Royal Meteorol. Soc.* **141**, 1035–1048 (2015).
- 358 32. Nie, J., Dai, P. & Sobel, A. H. Dry and moist dynamics shape regional patterns of extreme precipitation sensitivity. *Proc. Natl. Acad. Sci.* **117**, 8757–8763 (2020).
- 359 33. Sørland, S. L., Sorteberg, A., Liu, C. & Rasmussen, R. Precipitation response of monsoon low-pressure systems to an idealized uniform temperature increase. *J. Geophys. Res. Atmospheres* **121**, 6258–6272 (2016).
- 360 34. Shukla, J. Interannual variability of monsoons. *Monsoons* **14**, 399–464 (1987).
- 361 35. Mak, M. Synoptic-scale disturbances in the summer monsoon. *Monsoon meteorology* (1987).
- 362 36. Vijaykumar, P. *et al.* Kerala floods in consecutive years-its association with mesoscale cloudburst and structural changes in monsoon clouds over the west coast of india. *Weather. climate extremes* **33**, 100339 (2021).
- 363 37. Emori, S. & Brown, S. Dynamic and thermodynamic changes in mean and extreme precipitation under changed climate. *Geophys. Res. Lett.* **32** (2005).
- 364 38. Sugiyama, M., Shiogama, H. & Emori, S. Precipitation extreme changes exceeding moisture content increases in miroc and ipcc climate models. *Proc. Natl. Acad. Sci.* **107**, 571–575 (2010).
- 365 39. Knutson, T., Landsea, C. & Emanuel, K. Tropical cyclones and climate change: A review. *Glob. perspectives on tropical cyclones: from science to mitigation* 243–284 (2010).
- 366 40. Liu, M., Vecchi, G. A., Smith, J. A. & Knutson, T. R. Causes of large projected increases in hurricane precipitation rates with global warming. *npj Clim. Atmospheric Sci.* **2**, 1–5 (2019).
- 367 41. O’Gorman, P. A. Sensitivity of tropical precipitation extremes to climate change. *Nat. Geosci.* **5**, 697–700 (2012).
- 368 42. Pfahl, S., O’Gorman, P. A. & Fischer, E. M. Understanding the regional pattern of projected future changes in extreme precipitation. *Nat. Clim. Chang.* **7**, 423–427 (2017).
- 369 43. Nie, J., Sobel, A. H., Shaevitz, D. A. & Wang, S. Dynamic amplification of extreme precipitation sensitivity. *Proc. Natl. Acad. Sci.* **115**, 9467–9472 (2018).
- 370 44. Majda, A. J. & Shefter, M. G. Models for stratiform instability and convectively coupled waves. *J. atmospheric sciences* **58**, 1567–1584 (2001).
- 371 45. Arakawa, A. The cumulus parameterization problem: Past, present, and future. *J. Clim.* **17**, 2493–2525 (2004).
- 372 46. Diaz, M. & Boos, W. R. Barotropic growth of monsoon depressions. *Q. J. Royal Meteorol. Soc.* **145**, 824–844 (2019).
- 373 47. Cohen, N. Y. & Boos, W. R. Perspectives on moist baroclinic instability: Implications for the growth of monsoon depressions. *J. Atmospheric Sci.* **73**, 1767–1788 (2016).
- 374 48. Diaz, M. & Boos, W. R. Monsoon depression amplification by moist barotropic instability in a vertically sheared environment. *Q. J. Royal Meteorol. Soc.* **145**, 2666–2684 (2019).

- 394 49. Adames, Á. F. & Ming, Y. Moisture and moist static energy budgets of South Asian monsoon low pressure systems in
395 GFDL AM4. 0. *J. Atmospheric Sci.* **75**, 2107–2123 (2018).
- 396 50. Suhas, D. & Boos, W. R. Monsoon depression amplification by horizontal shear and humidity gradients: a shallow water
397 perspective. *J. Atmospheric Sci.* **80**, 633–647 (2023).
- 398 51. Goswami, B. N., Keshavamurty, R. & Satyan, V. Role of barotropic, baroclinic and combined barotropic-baroclinic
399 instability for the growth of monsoon depressions and mid-tropospheric cyclones. *Proc. Indian Acad. Sci. Planet. Sci.* **89**,
400 79–97 (1980).
- 401 52. Goswami, B. N., Ajayamohan, R., Xavier, P. K. & Sengupta, D. Clustering of synoptic activity by indian summer monsoon
402 intraseasonal oscillations. *Geophys. Res. Lett.* **30** (2003).
- 403 53. Luo, H., Adames-Corraliza, A. & Rood, R. B. Energy budget perspective on monsoon low pressure system growth by
404 barotropic and moisture-vortex instabilities. In *Fall Meeting 2022* (AGU, 2022).
- 405 54. Eyring, V. *et al.* Human influence on the climate system. in *climate change 2021: The physical science basis. contribution*
406 *of working group i to the sixth assessment report of the intergovernmental panel on climate change. IPCC Sixth Assess.*
407 *Rep.* (2021).
- 408 55. Douglas, A. P. & Hoadley, A. F. A. A process integration approach to the design of the two-and three-column methanol
409 distillation schemes. *Appl. thermal engineering* **26**, 338–349 (2006).
- 410 56. Cook, B. I., Puma, M. J. & Krakauer, N. Y. Irrigation induced surface cooling in the context of modern and increased
411 greenhouse gas forcing. *Clim. Dyn.* **37**, 1587–1600 (2011).
- 412 57. Shukla, S. P., Puma, M. J. & Cook, B. I. The response of the south asian summer monsoon circulation to intensified
413 irrigation in global climate model simulations. *Clim. dynamics* **42**, 21–36 (2014).
- 414 58. Huang, Z. *et al.* Reconstruction of global gridded monthly sectoral water withdrawals for 1971–2010 and analysis of their
415 spatiotemporal patterns. *Hydrol. Earth Syst. Sci.* **22**, DOI: [10.5194/hess-22-2117-2018](https://doi.org/10.5194/hess-22-2117-2018) (2018).
- 416 59. Vishnu, S., Boos, W. R., Ullrich, P. A. & O'Brien, T. A. Global track dataset of monsoon low pressure systems. *Zenodo*
417 <https://doi.org/10.5281/zenodo.3890646> (2020).
- 418 60. Hersbach, H. *et al.* Global reanalysis: goodbye ERA-Interim, hello ERA5. *ECMWF newsletter* **159**, 17–24 (2019).
- 419 61. CIESIN. Gridded Population of the World, Version 4 (GPWv4): Population Density Adjusted to Match 2015 Revision
420 UN WPP Country Totals, Revision 11. Palisades, NY. *NASA Socioeconomic Data and Applications Center (SEDAC)*
421 <https://doi.org/10.7927/H4F47M65> Accessed 29 January 2021 (2018).
- 422 62. Doxsey-Whitfield, E. *et al.* Taking advantage of the improved availability of census data: a first look at the gridded
423 population of the world, version 4. *Pap. Appl. Geogr.* **1**, 226–234 (2015).
- 424 63. Pai, D. *et al.* Development of a new high spatial resolution (0.25×0.25) long period (1901–2010) daily gridded rainfall
425 data set over India and its comparison with existing data sets over the region. *Mausam* **65**, 1–18 (2014).
- 426 64. Rajeevan, M., Bhate, J., Kale, J. & Lal, B. Development of a high resolution daily gridded rainfall data for the indian
427 region. *Met. Monogr. Climatol.* **22**, 2005 (2005).
- 428 65. Funk, C. *et al.* The climate hazards infrared precipitation with stations—a new environmental record for monitoring
429 extremes. *Sci. data* **2**, 1–21 (2015).
- 430 66. Ashouri, H. *et al.* Persiann-cdr: Daily precipitation climate data record from multisatellite observations for hydrological
431 and climate studies. *Bull. Am. Meteorol. Soc.* **96**, 69–83 (2015).
- 432 67. Willett, K. *et al.* Hadisdh land surface multi-variable humidity and temperature record for climate monitoring. *Clim. Past*
433 **10**, 1983–2006 (2014).
- 434 68. Smith, A., Lott, N. & Vose, R. The integrated surface database: Recent developments and partnerships. *Bull. Am. Meteorol.*
435 *Soc.* **92**, 704–708 (2011).
- 436 69. Data, C. Guidelines on analysis of extremes in a changing climate in support of informed decisions for adaptation. *World*
437 *Meteorol. Organ.* (2009).
- 438 70. Seabold, S. & Perktold, J. statsmodels: Econometric and statistical modeling with python. In *9th Python in Science*
439 *Conference* (2010).
- 440 71. Benjamini, Y. & Hochberg, Y. Controlling the false discovery rate: a practical and powerful approach to multiple testing. *J.*
441 *Royal statistical society: series B (Methodological)* **57**, 289–300 (1995).

- 442 **72.** Wilks, D. “the stippling shows statistically significant grid points”: How research results are routinely overstated and
443 overinterpreted, and what to do about it. *Bull. Am. Meteorol. Soc.* **97**, 2263–2273 (2016).

444 **Acknowledgements**

445 This material is based on work supported by the U.S. Department of Energy, Office of Science, Office of Biological and
446 Environmental Research, Climate and Environmental Sciences Division, Regional and Global Model Analysis Program, under
447 Award DE-SC0019367 and by the Director, Office of Science, Office of Biological and Environmental Research of the US
448 Department of Energy under contract numbers DEAC02-05CH11231 and DE-SC0010620. It used resources of the National
449 Energy Research Scientific Computing Center (NERSC), which is a DOE Office of Science User Facility. The authors also
450 acknowledge support from the Earth System Science Organization, Ministry of Earth Sciences, Government of India (Grant
451 IITM/MM-II/ Univ_California_USA/INT-3) to conduct this research under the Monsoon Mission.

452 **Author contributions statement**

453 S.V. and W.R.B. conceived the research, analyzed data, and wrote the manuscript. T.A.O. performed early data analysis and,
454 with P.A.U. and W.R.B., guided project direction. M.R. provided guidance on statistical methods. P.A.U. supported use of the
455 vortex-tracking software. All authors read and edited the manuscript.

456 **Additional information**

457 **Competing interests** (The authors declare no competing interests.).

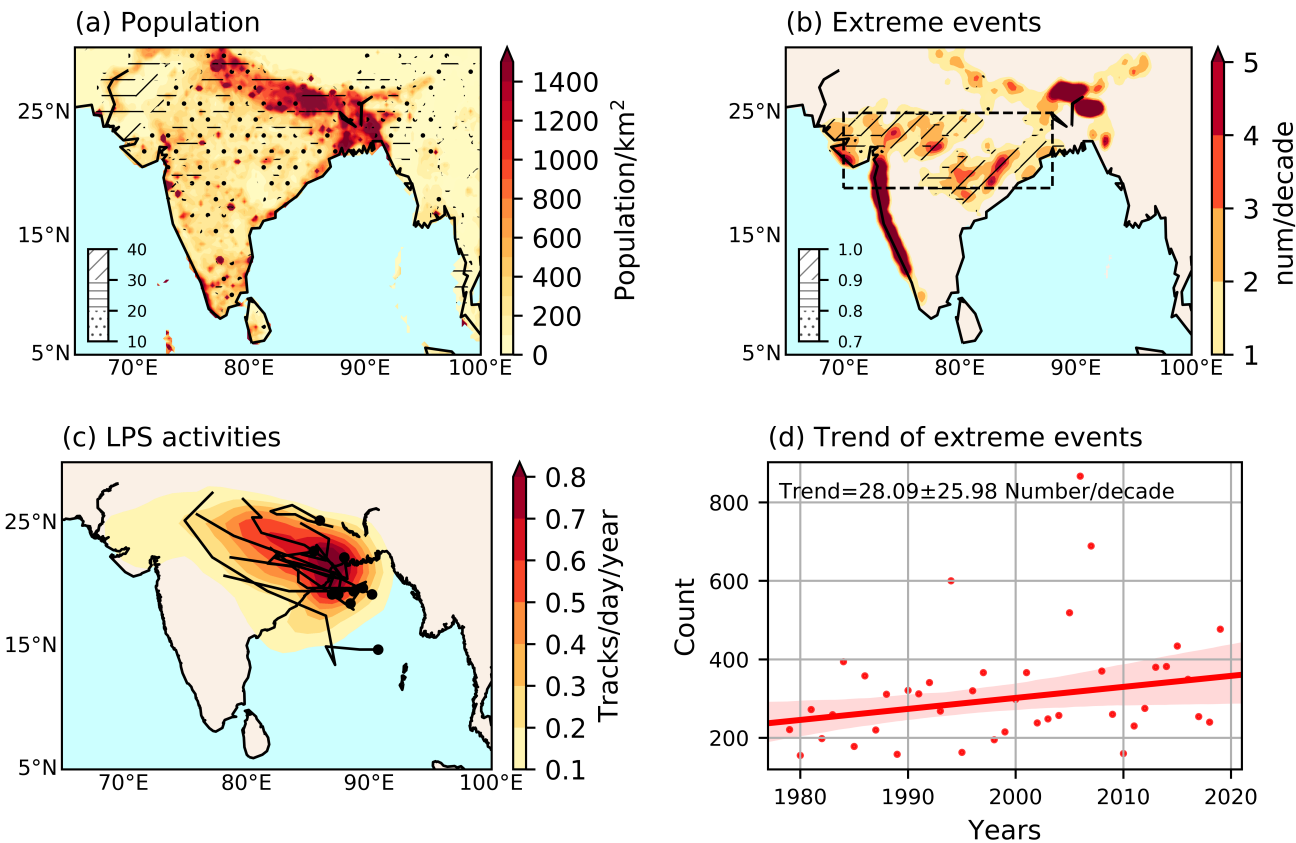


Figure 1. Importance of monsoon lows and depressions for human exposure to extreme precipitation. (a) Population density (shaded) and the percent growth between 2000–2020 (stippling/hatching). (b) Number of extreme precipitation events ($\geq 15 \text{ cm day}^{-1}$; see Methods) during summer (June–September, shaded) per decade and the fraction of these extreme events associated with LPS (stippling/hatching). (c) Track density of LPS for 1979–2019 from the ERA5 reanalyses (shading), with genesis points and tracks for 2018 (only one year is provided for clarity) shown as dots and lines, respectively. (d) Time series of the annual number of extreme precipitation events over central India (box in [b]) and its best linear fit; shading represents the 95% confidence interval for the fit, with the trend and the confidence interval for the slope marked in the figure. In (b) and (d), extreme rainfall events are derived from the IMD rainfall dataset at a horizontal resolution of 0.25° .

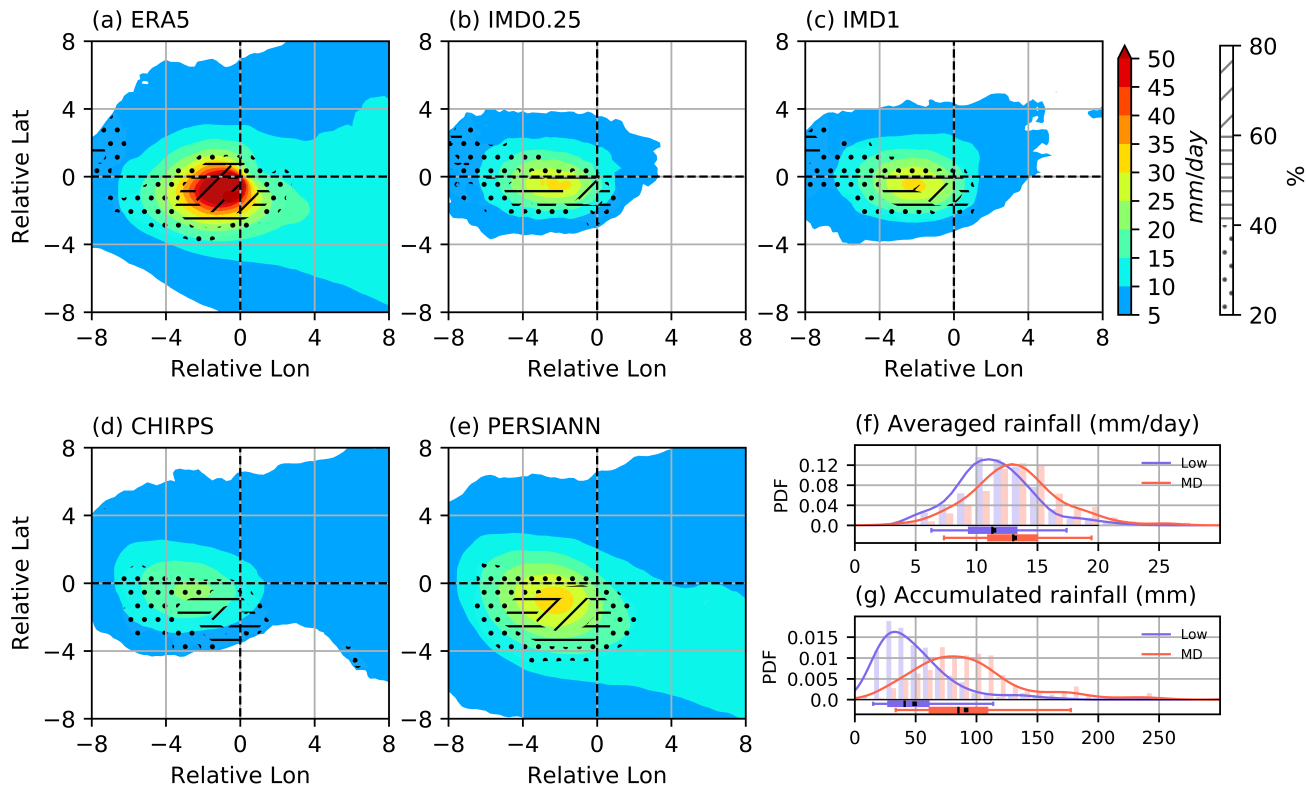


Figure 2. The distribution of precipitation in monsoon lows and depressions. Vortex-centered composites of precipitation in monsoon depressions for summer (June–September) 1979–2019 using data from (a) ERA5, (b) the high-resolution IMD (IMD0.25) dataset, (c) the low-resolution IMD (IMD1) dataset, (d) CHIRPS, and (e) PERSIANN. Stippling indicates the percentage by which the composite monsoon depression precipitation exceeds that of monsoon lows. Normalized histograms (bars), kernel density estimates of the probability distribution (curves), and box-whisker plots of (f) instantaneous and (g) track-accumulated precipitation for monsoon lows (purple) and monsoon depressions (red), all averaged over 8° circles around the vortex center with ERA5 precipitation. For the box-whisker plots, the vertical black line indicates the median, box boundaries indicate the 25th and 75th percentiles, whiskers indicate the 5th and 95th percentiles, and the solid square represents the mean.

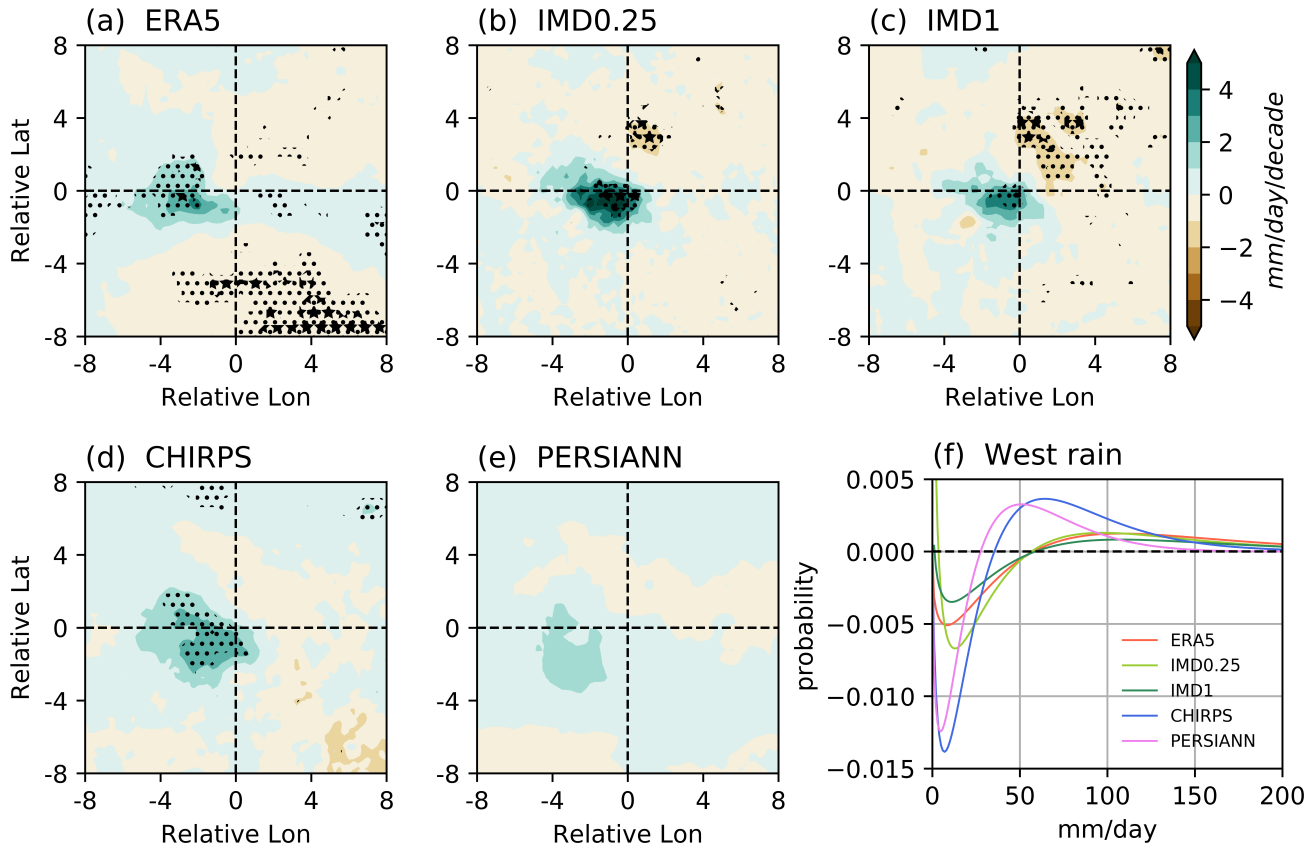


Figure 3. Observed increase in monsoon depression precipitation rates. Linear trend of vortex-centered precipitation in monsoon depressions in (a) ERA5, (b) the high resolution IMD (IMD0.25) dataset, (c) the low resolution IMD (IMD1) dataset, (d) CHIRPS, and (e) PERSIANN. Dots and stars mark points passing a false discovery rate test at the 33% and 15% level, respectively. (f) 40-year changes in the probability of precipitation in the heavily precipitating region of monsoon depressions (5°S - 5°N , 5°W - 0°E in vortex-centered coordinates) based on a statistical model that fits a gamma distribution to point-wise precipitation (see Methods).

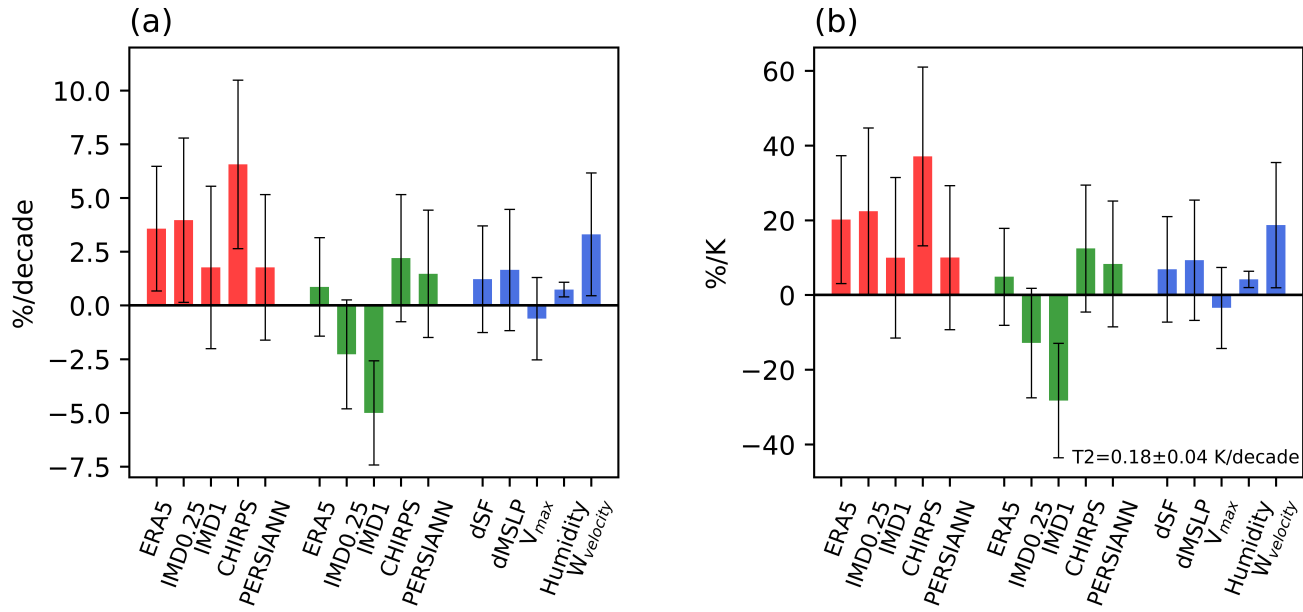


Figure 4. Bulk trends in rainfall and dynamical intensity of monsoon depressions. Linear trends in monsoon depression properties in (a) percentage per decade, (b) percentage per unit warming (%/K) of surface air over the tropical Indian Ocean ($20^{\circ}\text{S}-30^{\circ}\text{N}$, $50^{\circ}\text{E}-100^{\circ}\text{E}$). In both panels, red bars (left group) show the rainfall trend in the most heavily precipitating part of the storms ($2^{\circ}\text{S}-2^{\circ}\text{N}$, $5^{\circ}\text{W}-0^{\circ}\text{E}$ in vortex-centered coordinates) in all five precipitation datasets; green bars (middle group) show the trend in rainfall averaged within an 8° radius of the center; blue bars (right group) show trends in storm intensity metrics, specifically the strength of the minimum of the streamfunction of the 850 hPa horizontal wind (dSF), the strength of the minimum of the mean sea level pressure (dMSLP), and the surface wind speed maximum (V_{max}), together with trends in surface air specific humidity and lower-tropospheric vertical velocity in the heavily precipitating region. Error bars show a 90% confidence interval. Text in the bottom right in (b) is the slope of the linear trend of surface air temperature over the Tropical Indian Ocean, with a 90% confidence interval.

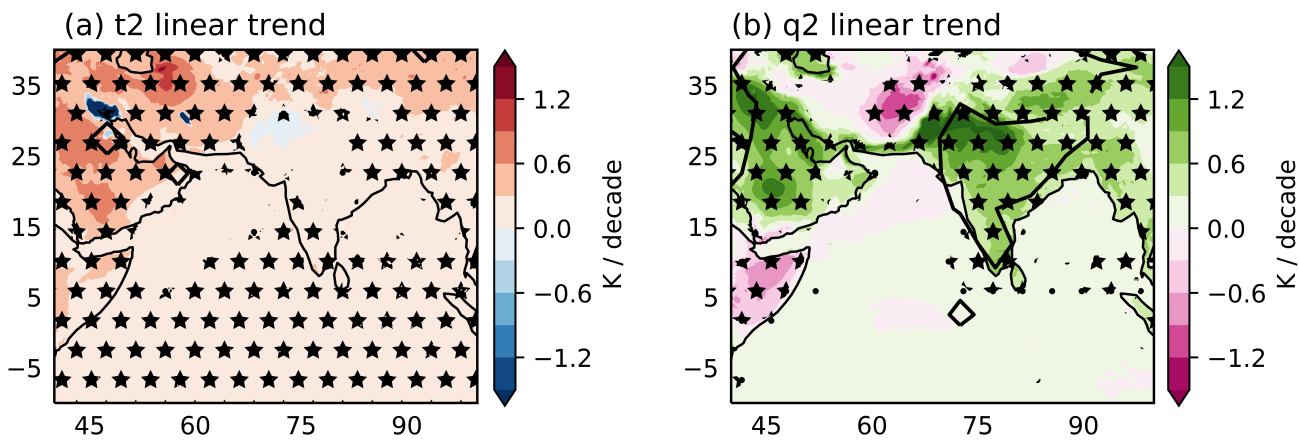


Figure 5. Rapid humidification and slow warming of South Asia. The linear trend of summer (June-September) mean values of (a) surface air temperature and (b) surface air specific humidity (converted to temperature units by multiplying by the ratio of the latent heat of vaporization to the specific heat of air), both in units of K decade^{-1} ; color shading shows ERA5 trends, while the black contour marks regions where the coarser-resolution gridded station data (HadISDH) trends are larger than $0.5 \text{ K decade}^{-1}$. Dots and stars mark points satisfying a 33% and 15% false discovery rate test, respectively.

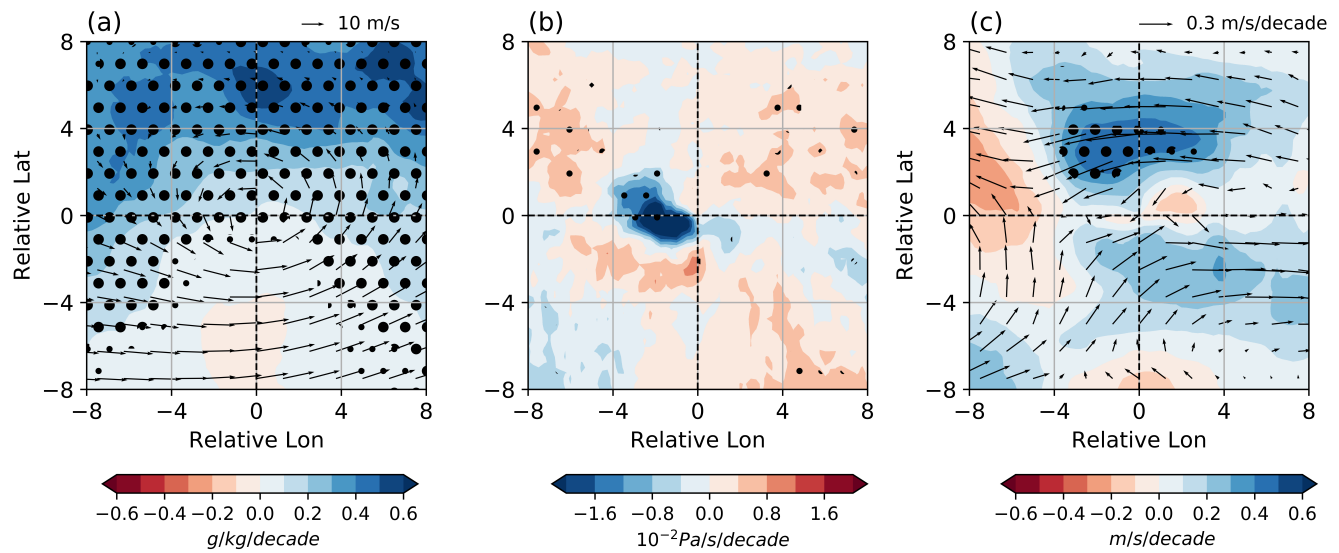


Figure 6. Trends in humidity, ascent, and horizontal circulation of monsoon depressions. For the composite monsoon depression, vortex-centered (a) linear trend in surface air specific humidity (shaded) with total (not trend) low-level (850 hPa) climatological wind (vectors) to illustrate the rotational flow, (b) linear trend in lower-tropospheric vertical velocity (925-700 hPa mean) and (c) linear trends in horizontal velocity (vector) and wind speed (shading) at 850 hPa (the level where the storm has the strongest horizontal circulation). Small and large dots mark points satisfying a false discovery rate test at 33% and 15%, respectively.

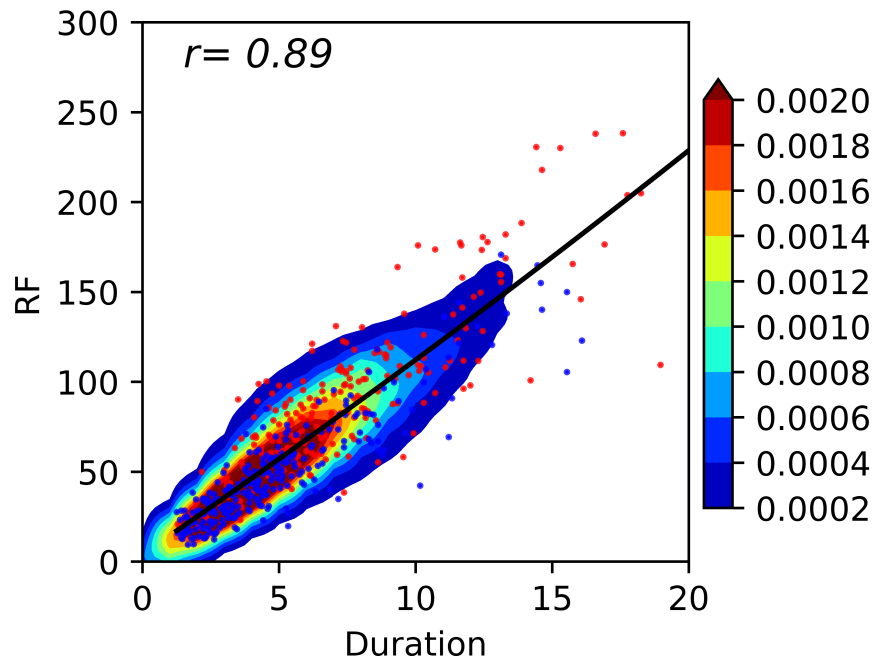


Figure S1. Relation of accumulated rainfall to low-pressure system lifetime. Scatter plot of accumulated rainfall along the track (mm) versus duration of LPS (days). Shading is a kernel density estimate of the joint distribution of these variables. Monsoon lows and monsoon depressions are marked by blue and red dots, respectively.

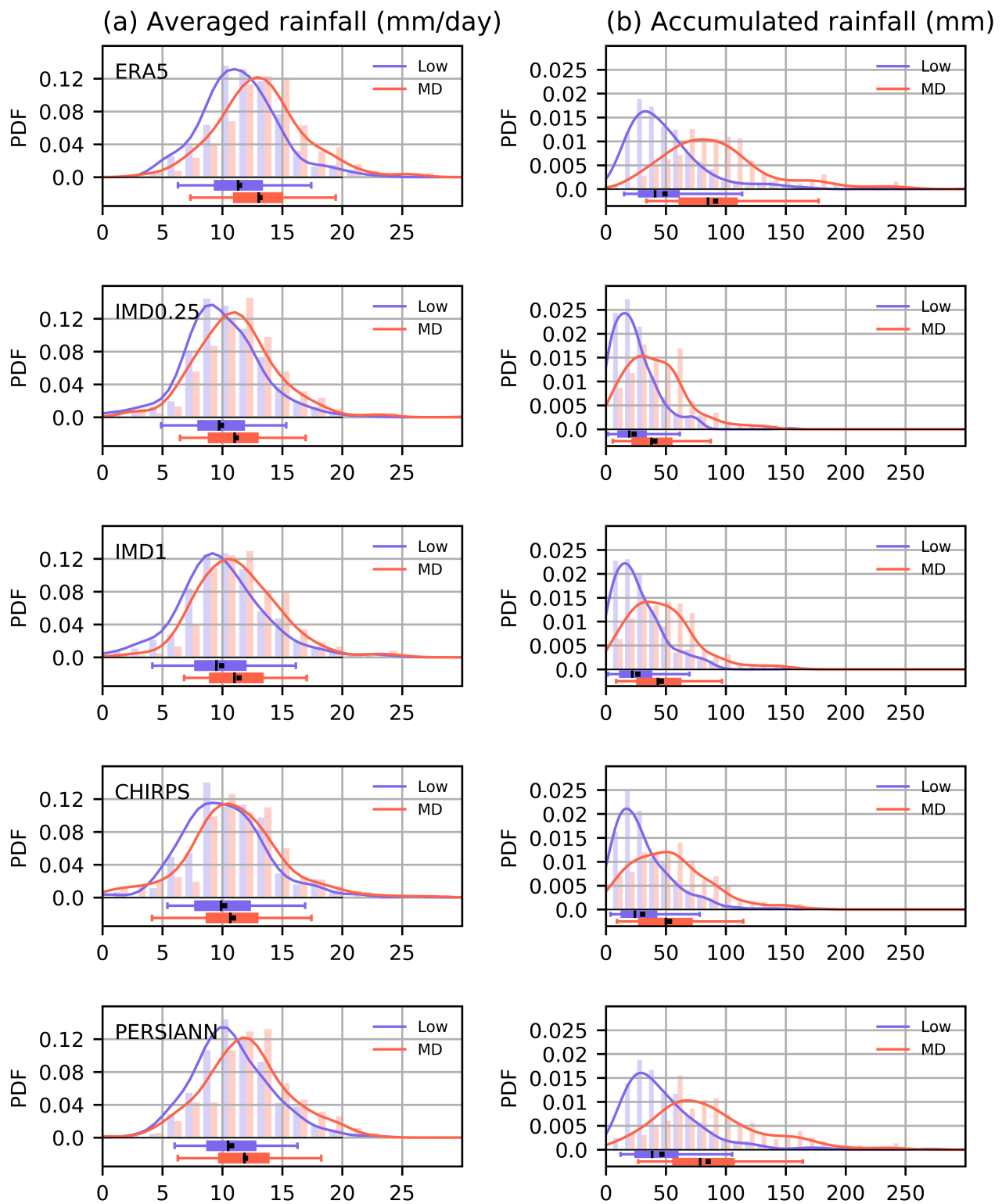


Figure S2. Probability of precipitation in monsoon lows and depressions in five datasets. As in Fig. 2f, g but for all five precipitation datasets, with the ERA5 plots repeated in the top panels for easier comparison.

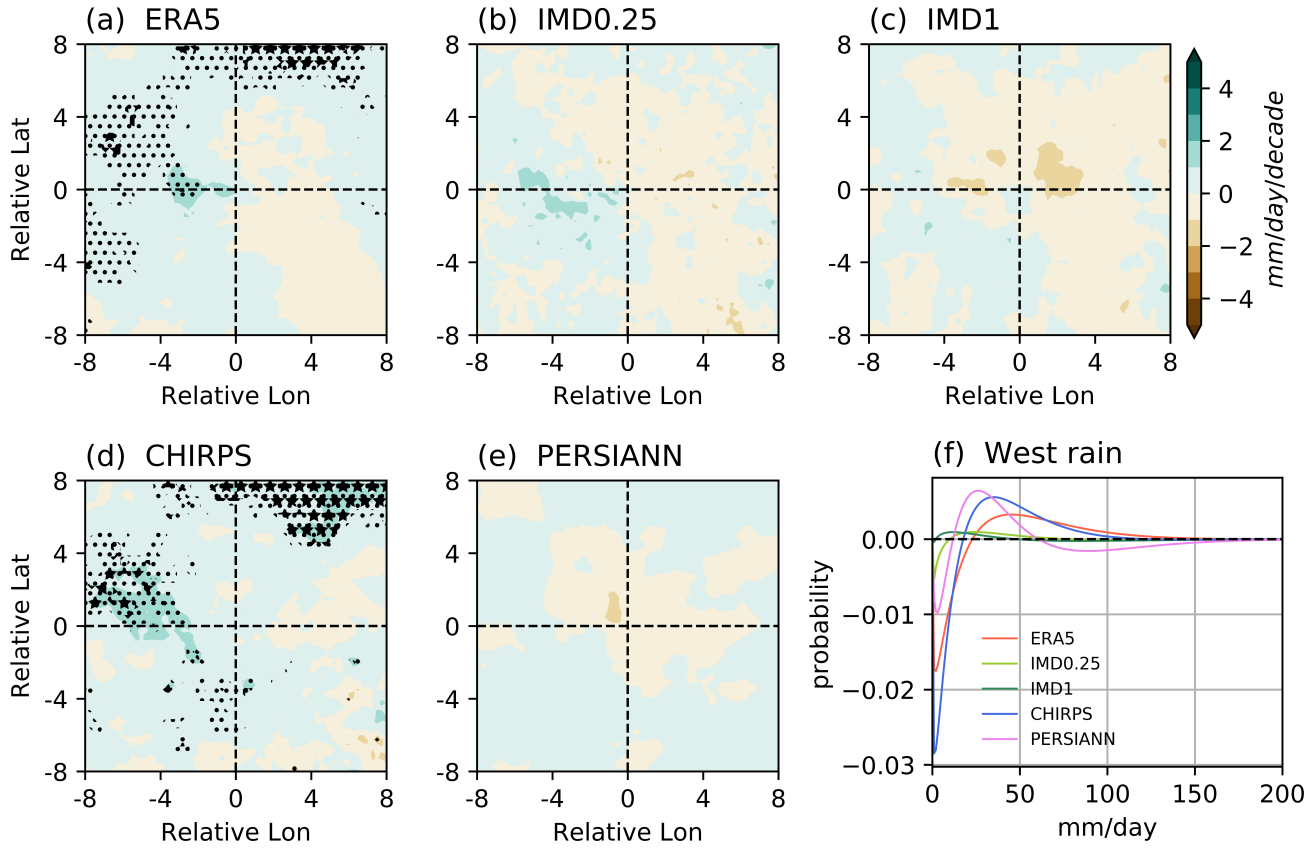


Figure S3. Observed increase in monsoon low precipitation rates. As in Fig. 3 but for monsoon lows.

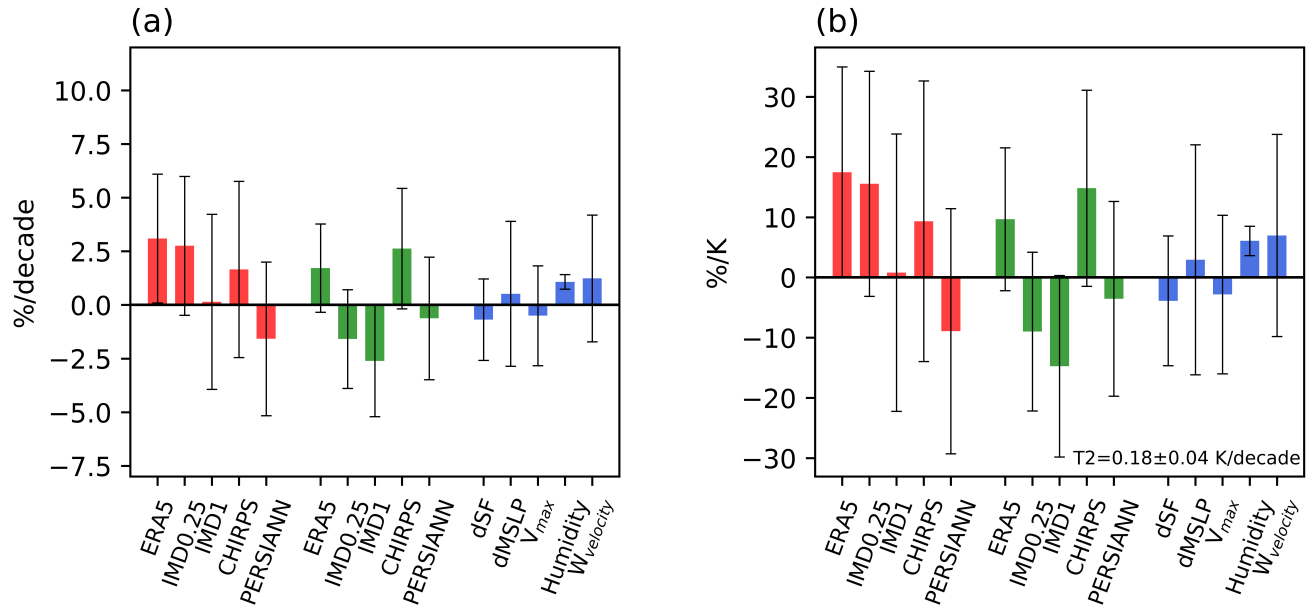


Figure S4. Bulk trends in rainfall and dynamical intensity of monsoon lows. As in Fig. 4 but for monsoon lows.

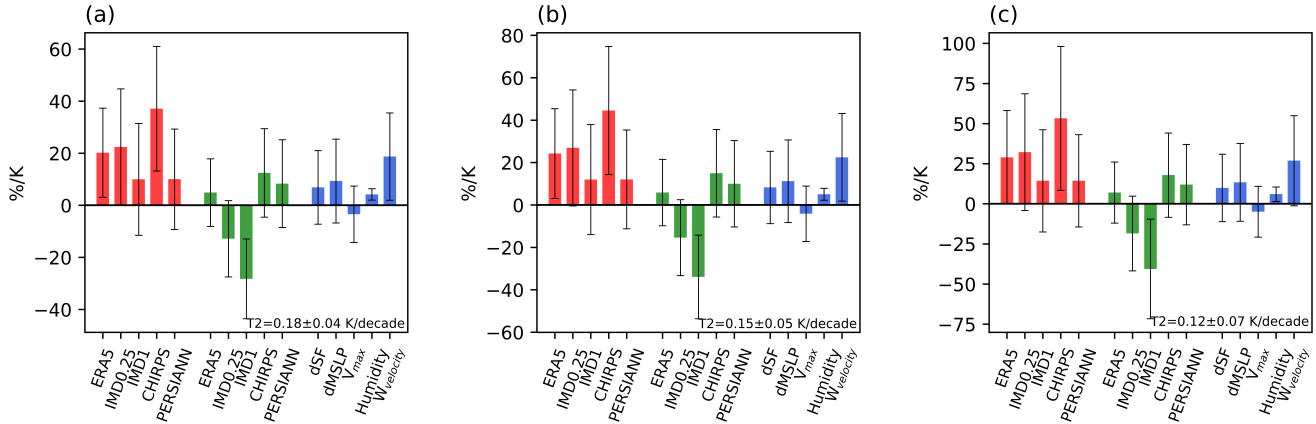


Figure S5. Sensitivity of temperature-normalized trends to region of warming. As in Fig. 4b but with the linear trends in monsoon depression properties normalized by the surface air temperature change averaged over different regions: (a) Tropical Indian Ocean ($20^{\circ}\text{S}-30^{\circ}\text{N}, 50^{\circ}\text{E}-100^{\circ}\text{E}$), (b) North Indian Ocean ($0^{\circ}\text{N}-30^{\circ}\text{N}, 50^{\circ}\text{E}-100^{\circ}\text{E}$), and (c) the region of highest track density for monsoon depressions ($15^{\circ}\text{N}-25^{\circ}\text{N}, 75^{\circ}\text{E}-95^{\circ}\text{E}$).

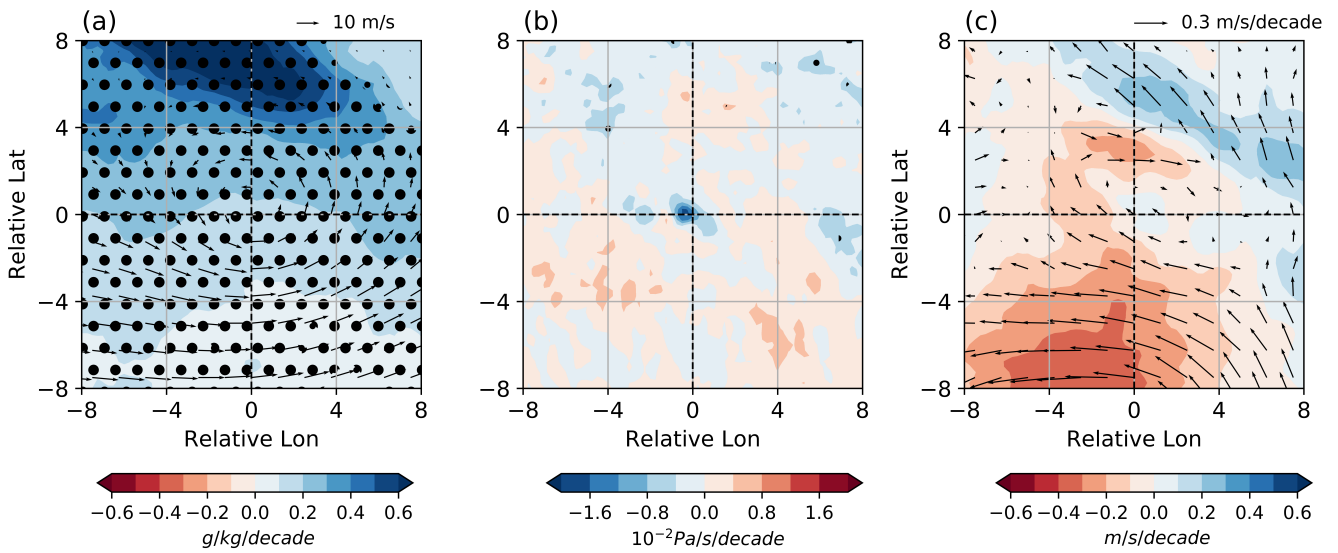


Figure S6. Trends in humidity, ascent, and horizontal circulation of monsoon lows. As in Fig. 6 but for monsoon lows.

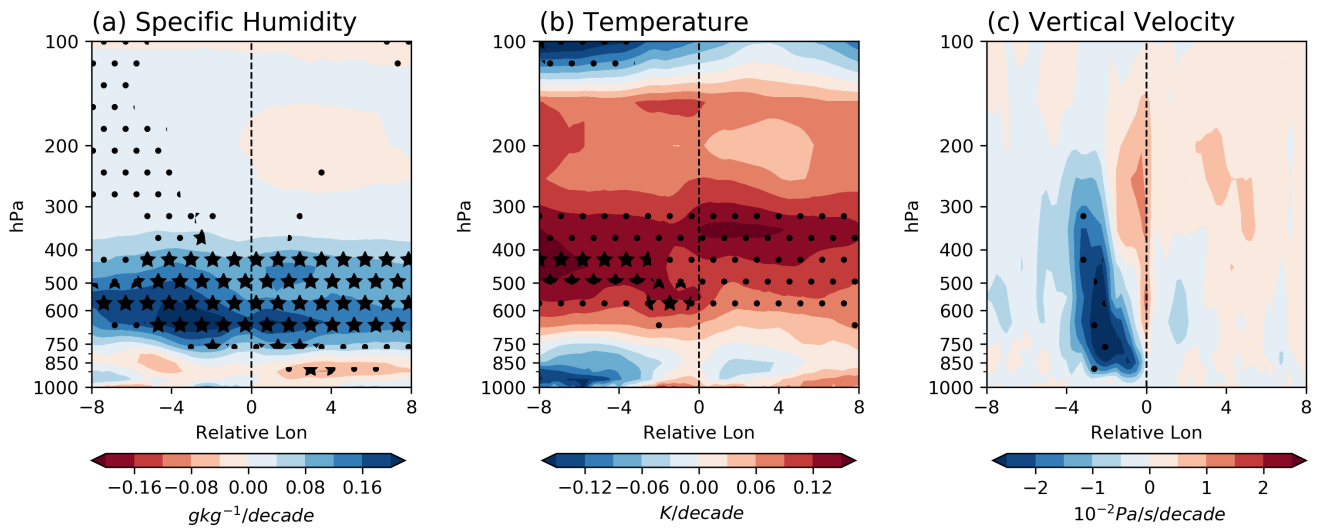


Figure S7. Vertical section of linear trends in humidity, temperature, and ascent. For the composite monsoon depression, linear trends through the central latitude of (a) specific humidity, (b) air temperature, and (c) vertical velocity. Dots and stars mark points satisfying a 33% and 15% false discovery rate test, respectively.

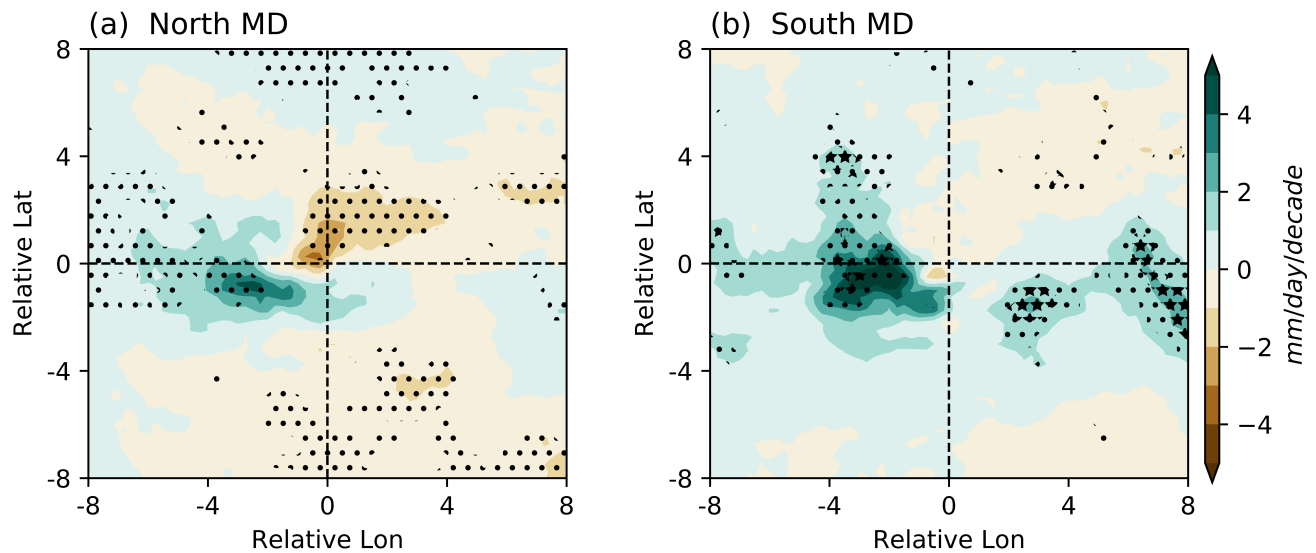


Figure S8. Similarity of rainfall trends between northern and southern monsoon depressions. Trend in ERA5 vortex-centered precipitation for monsoon depressions in two different geographic regions: (a) a northern box (22-30°N, 76-90°E) and (b) a southern box (13-22°N, 78-87°E). This analysis was motivated by a prior study showing that LPS tracks may have shifted southward over the past 40 years¹³ between these two boxes. Dots and stars mark points indicate points satisfying a 33% and 15% false discovery rate test, respectively.

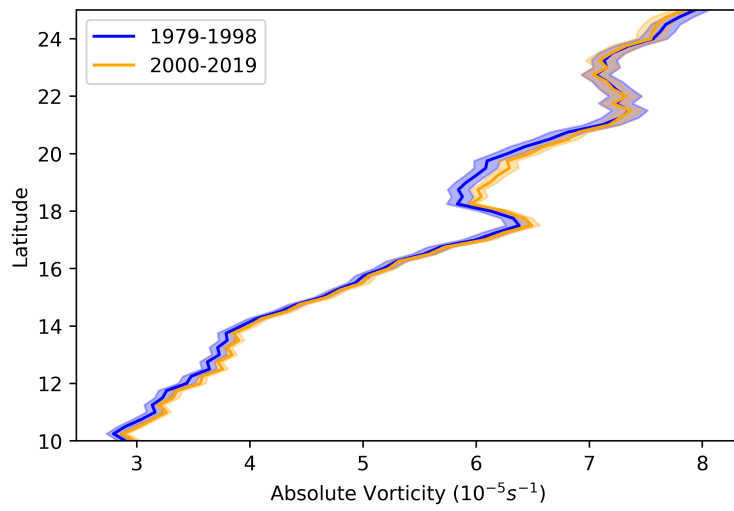


Figure S9. No large change in the low-level vorticity gradient. Comparison of latitudinal variation of absolute vorticity averaged over 80°E - 90°E at 850 hPa between the mean of the first twenty years (1979–1998, blue) and the last twenty years (2000–2019, orange). The shading represents the 90% confidence interval of the mean value.

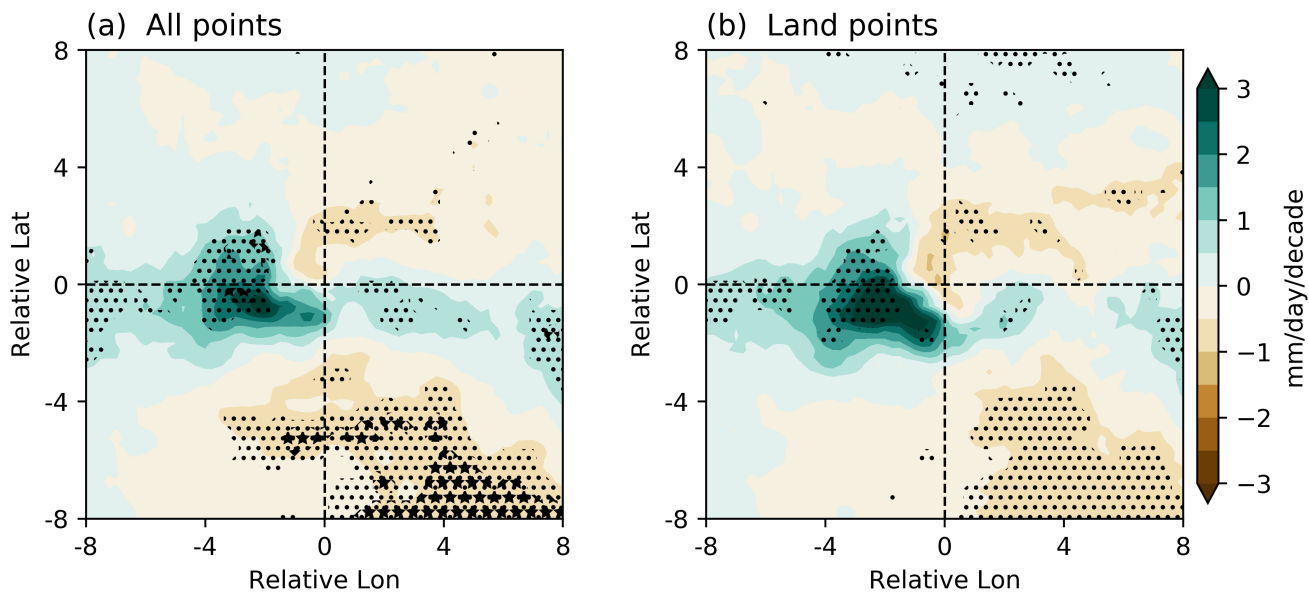


Figure S10. Monsoon depression precipitation rates over land vs. all land and ocean points. The linear trend of vortex-centred precipitation in monsoon depressions in ERA5 for (a) all points, including land and ocean, and (b) only land points. Dots and stars mark points passing a false discovery rate test at the 33% and 15% levels, respectively.